

1    **A new parameterization scheme of the real part of the ambient aerosols refractive index**

2    Gang Zhao<sup>1</sup>, Tianyi Tan<sup>2</sup>, Weilun Zhao<sup>1</sup>, Song Guo<sup>2</sup>, Ping Tian<sup>3</sup>, Chunsheng Zhao<sup>1\*</sup>

3    1 Department of Atmospheric and Oceanic Sciences, School of Physics, Peking University, Beijing,  
4    China

5    2 State Key Joint Laboratory of Environmental Simulation and Pollution Control, College of  
6    Environmental Sciences and Engineering, Peking University, Beijing 100871, China

7    3 Beijing Key Laboratory of Cloud, Precipitation and Atmospheric Water Resources, Beijing 100089,  
8    China

9    **\*Correspondence to: Chunsheng Zhao (zcs@pku.edu.cn)**

10    **Abstract**

11    The refractive index of ambient aerosols, which directly determines the aerosol optical properties,  
12    is widely used in atmospheric models and remote sensing. Traditionally, the real part of the refractive  
13    index (RRI) is mainly parameterized by the measurement of ambient aerosol main inorganic  
14    components. In this paper, the characteristics of the ambient aerosol RRI are studied based on the field  
15    measurement in the East China. Results show that the ambient aerosol RRI varies significantly between  
16    1.36 and 1.56. The direct aerosol radiative forcing is estimated to vary by 40% corresponding to the  
17    variation of the measured aerosol RRI. We find that the ambient aerosol RRI is highly correlated with  
18    the aerosol effective density ( $\rho_{\text{eff}}$ ) rather than the main chemical components. However,  
19    parameterization schemes of the ambient aerosol RRI by  $\rho_{\text{eff}}$  are not available due to the lack of  
20    corresponding simultaneous field measurements. For the first time, the size-resolved ambient aerosol

21 RRI and  $\rho_{\text{eff}}$  are measured simultaneously by our designed measurement system. A new  
22 parameterization scheme of the ambient aerosols RRI using  $\rho_{\text{eff}}$  is proposed. The measured and  
23 parameterized RRI agree well with the correlation coefficient of 0.75 and slope of 0.99. Knowledge of  
24 the ambient aerosol RRI would improve our understanding of the ambient aerosol radiative effects.

25 **1 Introduction**

26 Atmospheric aerosols can significantly influence the regional air quality and climate system by  
27 scattering and absorbing the solar radiation (Seinfeld et al., 1998). However, estimation of the aerosol  
28 radiative effects remains large uncertainties due to the high temporal and spatial variations in aerosol  
29 microphysical properties (Levoni et al., 1997). The complex refractive index (RI), which directly  
30 determines the aerosol scattering and absorbing abilities (Bohren and Huffman, 2007), is one of the  
31 most important microphysical parameters of aerosol optics and radiation. RI is widely employed in  
32 atmospheric models and remote sensing (Zhao et al., 2017). When estimating the direct aerosol  
33 radiative forcing (DARF), many studies showed that great uncertainties may arise due to small  
34 uncertainties in the real part of the RI (RRI). It was found that a small perturbation in RRI (0.003) can  
35 lead to an uncertainty of 1% in DARF for non-absorbing particles (Zarzana et al., 2014). An increment  
36 of 12% in the DARF occurred when the RRI increased from 1.4 to 1.5 (Moise et al., 2015) over the  
37 wavelength range between 0.2  $\mu\text{m}$  and 5  $\mu\text{m}$ . Therefore, it is necessary to measure or parameterize the  
38 ambient aerosol RRI with high accuracy.

39 Traditionally, the RRI is derived from measurements of aerosol main inorganic chemical  
40 compositions (Han et al., 2009). For the ambient aerosol with multiple components, linear volume  
41 average of known aerosol chemical composition is widely used to estimate the aerosol effective  
42  $RRI_{\text{eff}}$  (Hand and Kreidenweis, 2002; Liu and Daum, 2008; Hanel, 1968; Wex et al., 2002) with :

43 
$$RRI_{\text{eff}} = \sum_i (f_i \cdot RRI_i) \quad (1)$$

44 Where  $f_i$  and  $RRI_i$  are the volume fraction and real part of refractive index of known composition  
45  $i$ . However, the influences of organic component on the aerosol RRI were not considered when  
46 estimating the RRI using the traditional method. The organic component contributes more than 20%

47 of the total aerosol component in China (Hu et al., 2012; Liu et al., 2014). At the same time, RRI of the  
48 organic aerosol changes significantly between 1.36 and 1.66 (Moise et al., 2015). Ignoring the organic  
49 component may lead to significant biases when estimating the ambient aerosol RRI. The comparison  
50 between the estimated RRI using main aerosol composition and measured aerosol RRI using other  
51 method was not available due to the lack of measurement of ambient aerosol RRI.

52 Information of RRI may be helpful for the knowledge of ambient aerosol chemical information.  
53 Many studies find that ambient aerosols of different size have different properties such as shape (Peng  
54 et al., 2016), chemical composition (Hu et al., 2012) and density (Qiao et al., 2018). Up until now,  
55 there is limit information about the size-resolved RRI ( $\widetilde{RRI}$ ) of ambient particles. Characteristics of the  
56 ambient aerosol  $\widetilde{RRI}$  were not well studied yet.

57 The RRI of mono-component particle is defined as (Liu and Daum, 2008):

58 
$$\frac{RRI^2 - 1}{RRI^2 + 2} = \frac{N_A \alpha}{3M} \rho_{eff} \quad (2)$$

59 where  $N_A$  is the universal Avagadro's number,  $\alpha$  is the mean molecular polarizability,  $M$  is the  
60 molecular weight of the material and  $\rho_{eff}$  is the mass effective density of the chemical component.  
61 The RRI should be highly related to  $\rho_{eff}$ . However, there was no study that investigated the  
62 relationship between the RRI and  $\rho_{eff}$  of ambient aerosol in China.

63 The  $\rho_{eff}$  of ambient aerosols is one of the crucial parameters in aerosol thermo-dynamical and  
64 optical models. It can be used to infer the ambient particle aging process (Peng et al., 2016). Based on  
65 equation 2, the aerosol  $\rho_{eff}$  is directly related to the aerosol RRI. Few studies measure the ambient  
66 aerosol RRI and  $\rho_{eff}$  simultaneously. So far, parameterizations of the RRI by  $\rho_{eff}$  using the  
67 simultaneous measurements are not available. Real-time measurements of the  $\rho_{eff}$  and aerosol RRI  
68 concurrently can help to better understand the relationship between the aerosol RRI and  $\rho_{eff}$ .

69 In this study, the aerosol  $\widetilde{RRI}$  and size resolved  $\rho_{eff}$  ( $\widetilde{\rho_{eff}}$ ) are measured simultaneously during  
70 a field measurement conducted in Taizhou in the East China. The ambient aerosol  $\widetilde{RRI}$  is measured  
71 by our designed system, which combines a differential mobility analyzer (DMA) and a single particle  
72 soot photometer (SP2) (Zhao et al., 2019). The  $\widetilde{\rho_{eff}}$  is measured by using a centrifugal particle mass  
73 analyzer (CPMA) and a scanning mobility particle sizer (SMPS). The characteristic of the  $\widetilde{RRI}$  and  
74  $\widetilde{\rho_{eff}}$  are analyzed in this study. It is the first time that the  $\widetilde{RRI}$  and  $\widetilde{\rho_{eff}}$  of the ambient aerosol are

75 measured simultaneously. A parameterization scheme of the RRI by the  $\rho_{\text{eff}}$  using the simultaneous  
76 measurement is proposed. Based on the measured variability of the measured RRI, we estimated the  
77 corresponding variation of the aerosol direct aerosol radiative forcing, which to some extent give  
78 valuable knowledge for the influence of aerosol RRI variations on aerosol radiative effects.

79 The structure of this study is as follows: the descriptions of the instrument setup is given in section  
80 2.1, 2.2 and 2.3. The methodology of evaluating the aerosol optical properties and radiative effects  
81 corresponding to the variations of the measured RRI are shown in section 2.4 and 2.5 respectively.  
82 Section 3.1 describes the characteristics of the measured the  $\widetilde{\text{RRI}}$  and  $\widetilde{\rho_{\text{eff}}}$ . Section 3.3 proposes the  
83 parameterization of the aerosol RRI. The corresponding variations in aerosol optical properties and  
84 radiative effects corresponding to the variations of the measured RRI are both discussed in section 3.4.

## 85 **2 Data and Methods**

### 86 **2.1 Description of the measurement campaign**

87 The measurement was conducted in a suburban site Taizhou (119°57'E, 32°35'N), as shown in  
88 fig. 1(a), which lies in the south end of the Jianghuai Plain in the central Eastern China. It is located  
89 on the north east of the megacity Nanjing with a distance of 118 km. Another megacity Shanghai is  
90 200 km away from Taizhou in the southeastern direction. The industrial area between Nanjing and  
91 Shanghai has experienced severe pollutions in the past twenty years. The average Moderate Resolution  
92 Imaging Spectroradiometer (MODIS) aerosol optical depth data at 550nm over the year 2017, as  
93 shown in fig. 1(b), also reflects that the measurement site is more polluted than the surrounding areas.

94 During the field campaign, all of the instruments were placed in a container, in which the temperature  
95 was well controlled within  $24\pm2$  °C. The sample air was collected from a  $\text{PM}_{10}$  impactor (Mesa Labs,  
96 Model SSI2.5) mounted on the top of the container and then passed through a Nafion dryer tube to  
97 ensure that the relative humidity of the sample particles was controlled below 30%.

98 Along with the measurement of the  $\widetilde{\text{RRI}}$  and  $\widetilde{\rho_{\text{eff}}}$ , the aerosol scattering coefficients ( $\sigma_{\text{sca}}$ ) at three  
99 different wavelengths (450, 525 and 635 nm) were measured by an nephelometer (Aurora 3000,  
100 Ecotech, Australia) (Müller et al., 2011) at a resolution of 5 minutes. The scattering truncation and  
101 non-Lambertian error was corrected using the same method as that of Ma et al. (2011). The aerosol

102 water-soluble ions ( $\text{NH}_4^+$ ,  $\text{SO}_4^{2-}$ ,  $\text{NO}_3^-$ ,  $\text{Cl}^-$ ) of  $\text{PM}_{2.5}$  were measured by an In situ Gas and Aerosol  
103 Compositions Monitor (TH-GAC3000, China). The mass concentration of elementary carbon and  
104 organic carbon (OC) of  $\text{PM}_{2.5}$  were measured using a thermal optical transmittance aerosol carbon  
105 analyzer (ECOC, Focused Photonics Inc.). The concentrations of Organic matters (OM) are achieved  
106 through multiplying OC concentration by 1.4 (Hu et al., 2012). The time resolution of the aerosol  
107 composition measurement was one hour.

## 108 **2.2 Measuring the $\widetilde{\text{RRI}}$**

109 A coupling DMA-SP2 system was employed to measure the aerosol  $\widetilde{\text{RRI}}$  from 24<sup>th</sup>, May to 18<sup>th</sup>,  
110 June in 2018. This system is introduced elsewhere by (Zhao et al., 2019) and a brief description is  
111 presented here. As schematically shown in fig. 2, the monodispersed aerosols selected by a DMA  
112 (Model 3081, TSI, USA) are drawn into a SP2 to measure the corresponding scattering properties. The  
113 SP2 is capable of distinguishing the pure scattering aerosols from the black carbon (BC) containing  
114 aerosols by measuring the incandescence signals at 1064 nm. For the pure scattering aerosol, the  
115 scattering strength (S) measured by SP2 is expressed as:

116 
$$S = C \cdot I_0 \cdot (\sigma_{45^\circ} + \sigma_{135^\circ}) \quad (3),$$

117 where  $C$  is a constant that is determined by the instrument response character;  $I_0$  is the instrument's  
118 laser intensity;  $\sigma_{45^\circ}$  and  $\sigma_{135^\circ}$  is the scattering function of the sampled aerosol at  $45^\circ$  and  $135^\circ$ ,  
119 respectively;. From Mie scattering theory, aerosol size and RRI directly determine the scattering  
120 function at a given direction. Inversely, the aerosol RRI can be retrieved when the aerosol size and  
121 scattering strength are determined. This system can measure the ambient aerosol  $\widetilde{\text{RRI}}$  with uncertainty  
122 less than 0.02 (Zhao et al., 2019).

123 Before the measurement, this system is calibrated with ammonia sulfate ( $\text{RRI}=1.52$ ). After  
124 calibration, ammonium chloride is used to validate the method of deriving the RRI at different aerosol  
125 diameters. The RRI value of ammonium chloride is 1.642 (Lide, 2006) and the measured RRI of  
126 ammonium chloride is in the range between 1.624 and 1.656 in our study. Therefore, this measurement  
127 system can measure the ambient aerosol RRI with high accuracy.

## 128 **2.3 Measuring the $\widetilde{\rho_{\text{eff}}}$**

129 The  $\rho_{\text{eff}}$  is measured by a Centrifugal Particle Mass Analyzer (CPMA, version 1.53, Cambustion  
130 Ltd, UK) in tandem with a Scanning Mobility Particle Sizer (SMPS) system from 12<sup>th</sup>, June to 18<sup>th</sup>,  
131 June in 2018. The  $\rho_{\text{eff}}$  is defined as

132 
$$\rho_{\text{eff}} = \frac{m_p}{\frac{\pi}{6} \times d_m^3} \quad (4),$$

133 Where  $m_p$  is the particle mass and  $d_m$  is the aerosol mobility diameter selected by DMA.

134 The controlling of the CPMA-SMPS system is achieved by self-established Labview software.  
135 The CPMA is set to scan twelve different aerosol mass at 1.0, 1.4, 2.0, 2.9, 4.2, 5.9, 8.5, 12.1, 17.2,  
136 24.6, 35.0 and 50.0 fg every five minutes respectively. The SMPS scan the aerosol diameters between  
137 60nm and 500nm every 5 minute, which results in a period of one hour for measuring the effective  
138 density of different mass.

139 At the beginning of the field measurement, the CPMA-SMPS system is calibrated using the PSL  
140 particles with different mass. The corresponding measured effective densities of PSL particles are 1.04  
141 and 1.07 g/cm<sup>3</sup>, which agree well with the PSL material density of 1.05 g/cm<sup>3</sup>.

142 Fig. 3 gave three examples of the aerosol PNSDs that passed the CPMA and were measured by  
143 the SMPS. The mass values of the aerosol that can pass through the CPMA were set to be 12, 1 and  
144 1.4 fg respectively. From fig. 3, these aerosols that pass through the CPMA were mainly composed of  
145 three modes. For each mode, the aerosol number concentrations were fit by log-normal distribution  
146 function:

147 
$$N(H) = \frac{N_0}{\sqrt{2\pi} \log(\sigma_g)} \cdot \exp \left[ -\frac{\log Dp - \log(Dp)}{2 \log^2(\sigma_g)} \right], \quad (5)$$

148 where  $\sigma_g$  is the geometric standard deviation;  $Dp$  is the geometric mean diameter and  $N_0$  is the  
149 number concentrations for a peak mode. The geometric mean diameter is further analyzed.

150 We would demonstrate the mode 1, 2 and 3 in fig. 3 correspond to those aerosols of absorbing  
151 aerosol, scattering aerosol, and scattering aerosol with double charges respectively.

152 Based on the principle of CPMA, when the CPMA is selecting the aerosols at mass  $m_0$  of single  
153 charged aerosol particles. Theses multiple-charged (numbers of charges is  $n$ ) aerosol particles with

154 mass concentration of  $nm_0$  can pass through the CPMA at the same time. We assumed that the  
 155 geometric diameter of the single charge aerosol particles was  $D_0$ , and the effective density among  
 156 different aerosol diameter didn't have significant variations. Thus, the geometric diameter of the  
 157 multiple charged aerosol particles is  $\sqrt[3]{nm}$ .

158 As for the DMA, when a voltage ( $V$ ) is applied to the DMA, only a narrow size range of aerosol  
 159 particles, with the same electrical mobility ( $Z_p$ ) can pass through the DMA (Knutson and Whitby,  
 160 1975). The  $Z_p$  is expressed as:

$$161 \quad Z_p = \frac{Q_{sh}}{2\pi VL} \ln\left(\frac{r_1}{r_2}\right) \quad (6)$$

162 where  $Q_{sh}$  is the sheath flow rate;  $L$  is the length of the DMA;  $r_1$  is the outer radius of annular space  
 163 and  $r_2$  is the inner radius of the annular space. The aerosol  $Z_p$ , which is highly related to the aerosols  
 164 diameter ( $D_p$ ) and the number of elementary charges on the particle ( $n$ ), is defined as:

$$165 \quad Z_p = \frac{neC(D_p)}{3\pi\mu D_p} \quad (7)$$

166 where  $e$  is the elementary charge;  $\mu$  is the gas viscosity coefficient,  $C(D_p)$  is the Cunningham slip  
 167 correction that is defined by:

$$168 \quad C = 1 + \frac{2\tau}{D_p} (1.142 + 0.558e^{-\frac{0.999D_p}{2\tau}}) \quad (8)$$

169 where  $\tau$  is the gas mean free path.

170 Therefore, the electrical diameter  $Z_p(n)$  of the particles with  $n$  charges and diameters  $\sqrt[3]{nm}$  can  
 171 be calculated based on equation 5. Thus, the corresponding diameter ( $D_n$ ) measured by the DMA can  
 172 be calculated with electrical diameter  $Z_p(n)$  and single charged particle by using equation 5 again. The  
 173 relationship of the  $D_n$  and the aerosol diameter selected by the DMA can be determined by changing  
 174 the aerosol  $D_p$  and charge numbers. The results were shown in fig. 4.

175 The fit geometric diameters of mode 2 and mode 3 were also shown in fig. 4. From fig. 4, the  
 176 measured diameter relationships of the mode 2 and mode 3 agree well with the calculated one between  
 177 the single charged and double charged diameters. The little deviation might result from the

178 assumptions that the aerosol effective density doesn't change among different diameters. We  
179 concluded that the mode 3 corresponds to the double-charged aerosols. Mode 3 is not used in our study.

180 Mode 1 and mode 2 corresponding to the effective densities around  $1.0 \text{ g/cm}^3$  and  $1.5 \text{ g/cm}^3$ .  
181 Previous studies have shown that the ambient BC aerosol was chain like in the morphology and had  
182 smaller effective density values (Peng et al., 2016). At the same time, the fit aerosol number  
183 concentrations of mode one is only between 1/5 to 1/3 of the mode two. Based on the size-selected  
184 aerosol properties measured by the SP2, there were only mean 25% percent of the ambient aerosols  
185 that contains BC. Therefore, the mode 1 and mode 2 corresponded to the BC-contained aerosols and  
186 scattering aerosols respectively.

187 The effective density used in our study correspond to the geometric diameters of mode 2. Thus,  
188 both the measured aerosol effective density and RRI correspond to these scattering aerosols

#### 189 **2.4 Calculate aerosol optical properties using different RRI**

190 The aerosol optical properties are highly related to the RRI. From Mie scattering theory, the variation  
191 in aerosol RRI may result in significant variations in the aerosol optical properties, such as aerosol  
192 extinction coefficient ( $\sigma_{\text{ext}}$ ), the  $\sigma_{\text{sca}}$ , the single scattering albedo (SSA), and the asymmetry factor  
193 (g) (Bohren and Huffman, 2007). The  $\sigma_{\text{ext}}$ , SSA and g are the most important three factors that  
194 influence the aerosol radiative properties in radiative calculation (Kuang et al., 2015; Zhao et al., 2018).

195 In this study, the sensitivity studies of the aeorsol optical proprties to the aerosol RRI are carried  
196 out by employing the Mie scattering theory. The input variables of Mie scattering model includes the  
197 aerosol PNSD and BC mixing state and aerosol complex refractive index. The Mie model can calculate  
198 the  $\sigma_{\text{ext}}$ ,  $\sigma_{\text{sca}}$ , SSA and g. The mixing state of the ambient BC comes from the measurements of the  
199 DMA-SP2 system. All of the aerosols are divided into pure scattering aerosols and BC-containing  
200 aerosols. The BC-containing aerosols are assumed to be core-shell mixed. As for the RI of BC,  
201  $1.8+0.54i$  is used (Kuang et al., 2015). With this, the aerosol  $\sigma_{\text{ext}}$ ,  $\sigma_{\text{sca}}$ , SSA and g at different RRI  
202 values can be calculated.

#### 203 **2.5 Estimating the aerosol DARF**

204 In this study, the DARF under different aerosol RRI conditions is estimated by the Santa Barbara  
205 DISORT (discrete ordinates radiative transfer) Atmospheric Radiative Transfer (SBDART) model  
206 (Ricchiazzi et al., 1998). Under the cloud-free conditions, DARF at the TOA is calculated as the  
207 difference between radiative flux under aerosol-free conditions and aerosol present conditions  
208 (Kuang et al., 2016). The instant DARF value is calculated over the wavelength range between 0.25  
209  $\mu\text{m}$  and 4  $\mu\text{m}$ .

210 Input data for the model are shown below. The vertical profiles of temperature, pressure and water  
211 vapor, which adopt the radiosonde observations at Taizhou site. The measured mean results  
212 corresponding the field measurement period are used. Vertical distributions of aerosol  $\sigma_{\text{ext}}$ , SSA and  
213 g with a resolution of 50 m, are resulted from the calculation using the Mie Model and parameterized  
214 aerosol vertical distributions. Methods for parameterization and calculation of the aerosol optical  
215 profiles can be found in Zhao et al. (2018). The surface albedo adopt the mean results of MODIS V005  
216 Climate Modeling Grid (CMG) Albedo Product (MCD43C3) at the area of Taizhou from May, 2017  
217 to April, 2018. The other default values are used in the simulation (Ricchiazzi et al., 1998).

### 218 **3 Results and Discussions**

#### 219 **3.1 The Measurements Results**

220 The overview of the measurement is shown in fig. 5. During the measurement, the  $\sigma_{\text{sca}}$  is relatively  
221 low with a mean value of  $167 \pm 74 \text{ Mm}^{-1}$ . There were one major pollution episodes occurred based on  
222 the  $\sigma_{\text{sca}}$  time series as shown in fig. 5(a). This pollution happens on 13<sup>th</sup>, June and doesn't last long.  
223 The corresponding  $\sigma_{\text{sca}}$  reaches  $540 \text{ Mm}^{-1}$ . A moderate polluted condition between 14<sup>th</sup>, June and  
224 15<sup>th</sup>, June is observed. The aerosol PNSD changes substantially with the pollution conditions as  
225 shown in fig. 5(b). The geometric median aerosol diameter changes between 30 nm and 105 nm. The  
226 median diameter tends to be lower when the surrounding is cleaner. Despite the median diameter  
227 reaches 105 nm on 16<sup>th</sup>, June, the surrounding is relative clean due to the low aerosol number  
228 concentration. The  $\widetilde{\text{RRI}}$  varies from 1.34 to 1.54 and the  $\widetilde{\rho_{\text{eff}}}$  ranges between 1.21 to  $1.80 \text{ g/cm}^3$  as  
229 shown in fig. 5 (c) and (d). From fig. 5, the measured RRI shows the same variation pattern with the  
230  $\rho_{\text{eff}}$ . Both the  $\widetilde{\text{RRI}}$  and  $\widetilde{\rho_{\text{eff}}}$  increase with the diameter, which may indicate that the aerosol chemical  
231 composition varies among different aerosol particle size.

232 As for the  $\widetilde{RRI}$ , the corresponding mean RRI values for aerosol diameter at 200nm, 300nm and  
233 450nm are  $1.425 \pm 0.031$ ,  $1.435 \pm 0.041$ ,  $1.47 \pm 0.059$ . When comparing the probability distribution of the  
234 RRI for different diameter in fig. 6, the RRI is more dispersed when the particle size increases,  
235 implicating that the aerosol compositions become complicated when the aerosol get aged. Fig. 6 (a),  
236 (c) and (e) give diurnal variation of the  $\widetilde{RRI}$  values at different particle sizes of 200 nm, 300 nm and  
237 450 nm. The RRI shows diurnal cycles for different diameters. They reach the peak at about 15:00 in  
238 the afternoon and fall to the valley at around 9:00 in the morning.

239 The range of the measured RRI (1.34~1.56) is a little wider than the literature values. The past  
240 measurement of the ambient aerosol RRI values varies between 1.4 and 1.6 (Dubovik, 2002;Guyon et  
241 al., 2003;Zhang et al., 2016) over different measurement site. This is the first time that such high  
242 variations in ambient aerosol RRI were observed at one site.

243 The  $\widetilde{\rho_{eff}}$  shows almost the same diurnal variations as the  $\widetilde{RRI}$  as shown fig. S1. The diurnal  
244 variations of the  $\widetilde{\rho_{eff}}$  is more dispersed because the time period of measuring the  $\widetilde{\rho_{eff}}$  is shorter (7  
245 days) comparing with the time of  $\widetilde{RRI}$  (28 days). It is evident that the  $\rho_{eff}$  increased with particle  
246 size. The difference of  $\rho_{eff}$  among different particle size should be resulted from different  
247 contributions of chemical compositions, especially the OM. Based on the previous measurement of the  
248 size-resolved chemical compositions using a micro orifice uniform deposit impactors (MOUDI), the  
249 mass fraction of OM get decreased with the increment of aerosol diameter (Hu et al., 2012). At the  
250 same time, the effective density of OM is lower than the other main inorganic compositions.

### 251 **3.2 Aerosol Chemical Composition versus the RRI**

252 From equation (1) and (2), the aerosol RRI can be determined by aerosol chemical composition (Liu  
253 and Daum, 2008). Many studies calculate the RRI using the measurement results of the relative  
254 contributions of aerosol chemical composition (Yue et al., 1994;Hänel, 1968;Guyon et al.,  
255 2003;Stelson, 1990;Wex et al., 2002). However, there is no comparison between the RRI calculated  
256 from chemical composition and real-time measurement until now. In this study, the relationship  
257 between the measured RRI and the mass fraction of each ion components is investigated.

258 As illustrated in fig. 7, the RRI tend to increase with the OM mass fraction ratio, which implies that  
259 the OM may play an important role in aerosol scattering properties. This is in agreement with the

260 Aldhaif et al. (2018), where the aerosol OM contributes a lot to the ambient aerosol mass  
261 concentrations. The RRI have implicit relationship with the mass fraction of the  $\sigma_{\text{sca}}$  at 525 nm,  
262  $\text{SO}_4^{2-}$ ,  $\text{Cl}^-$ , and  $\text{NO}_3^-$ . The mass ratio of  $\text{NH}_4^+$  seems to be negatively correlated with the RRI. At  
263 the same time, the measured RRI values have no clear relationship with the absolute mass  
264 concentrations of the main aerosol chemical components, as shown in fig. S2.

265 The RRI is also calculated by applying the method proposed by Stelson (1990), in which the bulk  
266 chemical composition is used. The comparison between the calculated RRI and the measured RRI is  
267 shown in fig. 8. It can be noticed that the calculated RRI and the measured RRI doesn't agree well.  
268 There are several reasons that may cause the discrepancies. The first reason might be that the aerosol  
269 chemical information used in the method is the average mass of whole aerosol population. The aerosol  
270 chemical composition may vary significantly among different size. Secondly, the OM of the ambient  
271 aerosols is very complicated and the influence of the OM on the aerosol RRI has not been studied well.  
272 Therefore, more research is necessary when parameterizing the ambient aerosol RRI with the measured  
273 aerosol chemical composition.

274 We would demonstrate that the measured RRI at a given diameter of 250 nm is in consistent with  
275 that of the bulk aerosol optical properties derived RRI. The aerosol-effective RRI of bulk aerosol was  
276 retrieved by applying the Mie scattering theory to the aerosol particle number size distribution (PNSD),  
277 aerosol bulk scattering coefficient and aerosol absorbing coefficient data (Cai et al., 2011). Fig. 9  
278 shows the time series of measured and retrieved aerosol RRI. Results in fig. 9 show that the measured  
279 and calculated RRI shows good consistence with  $R^2 = 0.59$ . Therefore, the size-resolved aerosol RRI  
280 can be used to represent the bulk aerosol optical properties. The measured RRI at 250 nm and  
281 calculated aerosol RRI using the bulk aerosol main chemical composition should to some extent  
282 correlated with each other. However, as shown in fig. 8, the measured RRI at 250 nm and calculated  
283 RRI using the method Stelson (1990) has  $R^2$  of 0.07. Therefore, the ambient aerosol RRI calculated  
284 from bulk aerosol main inorganic component may lead to great uncertainties.

### 285 **3.3 Parameterizing the RRI using $\rho_{\text{eff}}$**

286 As shown in fig. 5, there is good consistence between the variation of the measured  $\widetilde{\text{RRI}}$  and  $\widetilde{\rho_{\text{eff}}}$ .  
287 When defining the specific refractive index  $\text{Re}$  with  $\text{Re} = \frac{\text{RRI}^2 - 1}{\text{RRI}^2 + 2}$ , we found that the  $\text{Re}$  is highly

288 correlated with  $\rho_{eff}$  by a  $R^2$  equaling 0.75 and slope 0.99 (fig. 10). The linear relationships between  
289 the Re and  $\rho_{eff}$  is:

290 
$$\frac{RRI^2 - 1}{RRI^2 + 2} = 0.18\rho_{eff} \quad (9).$$

291 The RRI can be calculated based on equation 6:

292 
$$RRI = \sqrt{\frac{1 + 0.36\rho_{eff}}{1 - 0.18\rho_{eff}}} \quad (10).$$

293 Based on equation 9 and fig. 10 the aerosol RRI can be parameterized by the  $\rho_{eff}$  with high accuracy  
294 and the uncertainties of the calculated RRI using equation 10 can be constrained within 0.025. The  
295 aerosol  $\rho_{eff}$  is easier to be measured, and equation 10 might be used as a good probe of parameterizing  
296 the RRI.

297 To demonstrate the universality of this parameterization scheme, we conducted another  
298 measurement in the campus of Peking University (PKU) (N39°59', E116°18'), in North China Plain,  
299 where the aerosol effective density and real part of the refractive index are measured concurrently from  
300 16<sup>th</sup> to 20<sup>st</sup>, December in 2018. The RRI were also calculated using the parameterization scheme  
301 equation 7. The slope and correlation coefficient at PKU site are 0.97 and 0.56 respectively. The  
302 calculated and measured RRI show good consistence. Therefore, this scheme is applicable for different  
303 seasons at both Center China and North China Plain. We also compared the measured RRI and  
304 calculated RRI using the measured  $\rho_{eff}$  that have been previously published (Hänel, 1968; Tang and  
305 Munkelwitz, 1994; Tang, 1996; Hand and Kreidenweis, 2002; Guyon et al., 2003). The measured and  
306 calculated RRI show good consistence with  $R^2$  of 0.91 and slope of 1.0. Therefore, our  
307 parameterization scheme is universal and applicable.

308 This parameterization scheme is easy to use because the effective density is the only parameter used  
309 as input. We have demonstrated that the traditional method of calculating the RRI using aerosol main  
310 chemical components can have significant bias because the effects of organic aerosol is not considered.  
311 The RRI can be easy to calculate based on our parameterization scheme, as the effective density of  
312 ambient aerosol is rather easier to measure.

313 In the previous, Liu and Daum (2008) summarized some of the measured RRI and the  $\rho_{\text{eff}}$ , and  
314 parameterized the RRI as

315 
$$\frac{\text{RRI}^2 - 1}{\text{RRI}^2 + 2} = 0.23\rho^{0.39} \quad (8).$$

316 The feasibility of this scheme is tested here and the results are shown in fig. 8. The measured and  
317 parameterized RRI using the method of Liu and Daum (2008) deviated from 1:1 line. The relationship  
318 of the effective density and RRI were mainly from 4000 pure materials and few ambient aerosol data.  
319 However, the ambient aerosol were far from pure materials. At the same time, most of the pure  
320 materials have negligible contribution to the total aerosol. Therefore, the parameterization scheme  
321 from Liu and Daum (2008) can't well describe the relationships of the effective density and RRI of  
322 ambient aerosol.

323 **3.4 Influence of RRI Variation on Aerosol Optical Properties and Radiative Properties**

324 The measured RRI varies between 1.34 and 1.56 during the field campaign. The corresponding  
325 aerosol optical properties are estimated. When estimating the aerosol optical properties with different  
326 aerosol RRI, the measured mean aerosol PNSD and mixing states are used. Fig. 11 gives the variation  
327 of the aerosol  $\sigma_{\text{sca}}$ , SSA and g. From fig. 11, the  $\sigma_{\text{sca}}$  varies from  $162 \text{ Mm}^{-1}$  to  $308 \text{ Mm}^{-1}$ . The SSA  
328 varies between 0.843 and 0.895, which matches the variations of the dry aerosol SSA for different  
329 aerosol size distributions in the North China Plain (NCP) (Tao et al., 2014). As for the aerosol g, it  
330 decreases from 0.667 to 0.602 with the increment of the aerosol RRI. The ambient g values in the NCP  
331 are found within 0.55 and 0.66 (Zhao et al., 2018). Thus, the variations of the RRI have significant  
332 influence on the g. The aerosol optical properties change significantly with the variation of the ambient  
333 aerosol RRI.

334 The instant DARF values under different RRI are also estimated and the results are illustrated in fig.  
335 11(b). When the aerosol RRI increases from 1.4 to 1.5, the DARF varies from -6.17 to -8.35,  
336 corresponding to 15% variation in DARF. This values are in accordance with the work of Moise et al.  
337 (2015), who estimate that an increment of 12% in the DARF occurs when the RRI varies from 1.4 to  
338 1.5. The DARF can change from  $-4.9 \text{ w/m}^2$  to  $-10.14 \text{ w/m}^2$  when the aerosol RRI increase from 1.34  
339 to 1.56, which corresponding to 40% variation in DARF. Great uncertainties may arise when  
340 estimating the aerosol radiative forcing when using a constant RRI. The RRI should be different under

341 different aerosol conditions. The real time measured RRI should be used rather than a constant RRI  
342 when estimating the ambient aerosol optical and radiative properties. However, the real-time  
343 measurement of ambient aerosol RRI is not available for most of the conditions. Our proposed  
344 parameterizations scheme is a perfect substitute. The only parameter required is aerosol effective  
345 density and it is much easier to measure.

346 **4 Conclusions**

347 The ambient aerosol RRI is a key parameter in determining the aerosol optical properties and  
348 knowledge of it can help constrain the uncertainties in aerosol radiative forcing. In this study, the  
349 ambient aerosol  $\widetilde{RRI}$  were measured at Taizhou, in the Jianghuai Plain of China by using a DMA in  
350 tandem with a SP2 from 24<sup>th</sup>, May to 18<sup>th</sup>, June in 2018.

351 Results show that the ambient aerosol RRI varies over a wide range between 1.34 and 1.56. The  
352 RRI increases slowly with the increment of the aerosol diameter. The mean aerosol RRI values are  
353  $1.425 \pm 0.031$ ,  $1.435 \pm 0.041$ ,  $1.47 \pm 0.059$  for aerosol diameter at 200 nm, 300 nm and 450 nm  
354 respectively. Probability distributions of the RRI show that the RRI is more dispersed with the  
355 increment of aerosol diameter, which reflect the complexing aging processing of the ambient aerosol.  
356 The aerosol optical properties change significantly and the DARF is estimated to vary by 40%  
357 corresponding to the variation of the measured ambient aerosol RRI. The real-time measured RRI  
358 should be used rather than a constant RRI when estimating the ambient aerosol optical and radiative  
359 properties.

360 Traditionally, the ambient aerosol RRI is mainly calculated by using the corresponding measured  
361 main chemical inorganic compositions of aerosols. We find that the ambient aerosol RRI is highly  
362 correlated with the  $\rho_{eff}$  rather than the main chemical compositions of aerosols. There is discrepancy  
363 between the measured and parameterized RRI using the traditional method. This might be resulted  
364 from two reasons. The first one is that the aerosol chemical information used for calculation is the total  
365 aerosol loading. The aerosol chemical compositions may change significantly among different size.  
366 Another one is that the influence of OM of ambient aerosols is not considered. The RRI of OM varies  
367 significantly for different compositions (Moise et al., 2015).

368       Despite that the RRI is correlated with the  $\rho_{eff}$ , parameterization scheme of the ambient aerosol  
369       RRI using  $\rho_{eff}$  is not available due to the lack of simultaneously measurement. For the first time, the  
370       RRI and  $\rho_{eff}$  were measured simultaneously using our designed system. The  $\rho_{eff}$  is measured  
371       during the field campaign by employing a CMPS and a SMPS from 12<sup>th</sup>, June to 18<sup>th</sup>, June in 2018.

372       A new parameterization scheme of the ambient aerosol RRI using the  $\rho_{eff}$  is proposed based on  
373       the field measurement results. The measured and parameterized RRI agree well with the correlation  
374       coefficient of 0.75 and slope of 0.99. This parameterization scheme is validated at another  
375       measurement site at different season. This simple scheme is reliable and ready to be used in the  
376       calculation of aerosol optical and radiative properties. The corresponding measurement results can also  
377       be further used in climate model.

378

379       **Competing interests.** The authors declare that they have no conflict of interest.

380       **Data availability.** The data used in this study is available when requesting the authors.

381       **Author contributions.** GZ, CZ, WZ and SG designed and conducted the experiments; PT, TY and  
382       GZ discussed the results.

383       **Acknowledgments.** This work is supported by the National Natural Science Foundation of China  
384       (41590872) and National Key R&D Program of China (2016YFC020000:Task 5).

385       **References**

386       Aldhaif, A. M., Stahl, C., Braun, R. A., Moghaddam, M. A., Shingler, T., Crosbie, E., Sawamura, P.,  
387       Dadashazar, H., Ziemb, L., Jimenez, J. L., Campuzano-Jost, P., and Sorooshian, A.: Characterization  
388       of the Real Part of Dry Aerosol Refractive Index Over North America From the Surface to 12 km,  
389       Journal of Geophysical Research: Atmospheres, 10.1029/2018jd028504, 2018.  
390       Bohren, C. F., and Huffman, D. R.: Absorption and Scattering by a Sphere, in: Absorption and  
391       Scattering of Light by Small Particles, Wiley-VCH Verlag GmbH, 82-129, 2007.

392 Cai, Y., Montague, D. C., and Deshler, T.: Comparison of measured and calculated scattering from  
393 surface aerosols with an average, a size-dependent, and a time-dependent refractive index, Journal of  
394 Geophysical Research, 116, 10.1029/2010jd014607, 2011.

395 Dubovik, O.: Variability of absorption and optical properties of key aerosol types observed in  
396 worldwide locations, J.atmos.sci, 59, 590-608, 2002.

397 Guyon, P., Boucher, O., Graham, B., Beck, J., Mayol-Bracero, O. L., Roberts, G. C., Maenhaut, W.,  
398 Artaxo, P., and Andreae, M. O.: Refractive index of aerosol particles over the Amazon tropical forest  
399 during LBA-EUSTACH 1999, Journal of Aerosol Science, 34, 883-907, 10.1016/s0021-  
400 8502(03)00052-1, 2003.

401 Han, Y., Lü, D., Rao, R., and Wang, Y.: Determination of the complex refractive indices of aerosol  
402 from aerodynamic particle size spectrometer and integrating nephelometer measurements, Applied  
403 Optics, 48, 4108-4117, 10.1364/AO.48.004108, 2009.

404 Hand, J. L., and Kreidenweis, S. M.: A New Method for Retrieving Particle Refractive Index and  
405 Effective Density from Aerosol Size Distribution Data, Aerosol Sci. Technol., 36, 1012-1026,  
406 10.1080/02786820290092276, 2002.

407 Hänel, G.: REAL PART OF MEAN COMPLEX REFRACTIVE INDEX AND MEAN DENSITY OF  
408 SAMPLES OF ATMOSPHERIC AEROSOL PARTICLES, Tellus, 20, 371-&,  
409 10.3402/tellusa.v20i3.10016, 1968.

410 Hu, M., Peng, J., Sun, K., Yue, D., Guo, S., Wiedensohler, A., and Wu, Z.: Estimation of size-resolved  
411 ambient particle density based on the measurement of aerosol number, mass, and chemical size  
412 distributions in the winter in Beijing, Environ Sci Technol, 46, 9941-9947, 10.1021/es204073t, 2012.

413 Knutson, E. O., and Whitby, K. T.: Aerosol classification by electric mobility: apparatus, theory, and  
414 applications, Journal of Aerosol Science, 6, 443-451, [https://doi.org/10.1016/0021-8502\(75\)90060-9](https://doi.org/10.1016/0021-8502(75)90060-9),  
415 1975.

416 Kuang, Y., Zhao, C. S., Tao, J. C., and Ma, N.: Diurnal variations of aerosol optical properties in the  
417 North China Plain and their influences on the estimates of direct aerosol radiative effect, Atmos. Chem.  
418 Phys., 15, 5761-5772, 10.5194/acp-15-5761-2015, 2015.

419 Kuang, Y., Zhao, C. S., Tao, J. C., Bian, Y. X., and Ma, N.: Impact of aerosol hygroscopic growth on  
420 the direct aerosol radiative effect in summer on North China Plain, *Atmospheric Environment*, 147,  
421 224-233, 2016.

422 Levoni, C., Cervino, M., Guzzi, R., and Torricella, F.: Atmospheric aerosol optical properties: a  
423 database of radiative characteristics for different components and classes, *Appl Opt*, 36, 8031-8041,  
424 1997.

425 Lide, D. R.: *Handbook of Chemistry and Physics*, 86th Edition Edited(National Institute of Standards  
426 and Technology), *Journal of the American Chemical Society*, 128, 5585-5585, 10.1021/ja059868l,  
427 2006.

428 Liu, H. J., Zhao, C. S., Nekat, B., Ma, N., Wiedensohler, A., van Pinxteren, D., Spindler, G., Müller,  
429 K., and Herrmann, H.: Aerosol hygroscopicity derived from size-segregated chemical composition and  
430 its parameterization in the North China Plain, *Atmospheric Chemistry and Physics*, 14, 2525-2539,  
431 10.5194/acp-14-2525-2014, 2014.

432 Liu, Y., and Daum, P. H.: Relationship of refractive index to mass density and self-consistency of  
433 mixing rules for multicomponent mixtures like ambient aerosols, *Journal of Aerosol Science*, 39, 974-  
434 986, 10.1016/j.jaerosci.2008.06.006, 2008.

435 Ma, N., Zhao, C. S., Nowak, A., Müller, T., Pfeifer, S., Cheng, Y. F., Deng, Z. Z., Liu, P. F., Xu, W.  
436 Y., Ran, L., Yan, P., Göbel, T., Hallbauer, E., Mildenberger, K., Henning, S., Yu, J., Chen, L. L., Zhou,  
437 X. J., Stratmann, F., and Wiedensohler, A.: Aerosol optical properties in the North China Plain during  
438 HaChi campaign: an in-situ optical closure study, *Atmos. Chem. Phys.*, 11, 5959-5973, 10.5194/acp-  
439 11-5959-2011, 2011.

440 Moise, T., Flores, J. M., and Rudich, Y.: Optical properties of secondary organic aerosols and their  
441 changes by chemical processes, *Chemical Reviews*, 115, 4400-4439, 2015.

442 Müller, T., Laborde, M., Kassell, G., and Wiedensohler, A.: Design and performance of a three-  
443 wavelength LED-based total scatter and backscatter integrating nephelometer, *Atmos. Meas. Tech.*, 4,  
444 1291-1303, 10.5194/amt-4-1291-2011, 2011.

445 Peng, J., Hu, M., Guo, S., Du, Z., Zheng, J., Shang, D., Levy Zamora, M., Zeng, L., Shao, M., Wu, Y.-  
446 S., Zheng, J., Wang, Y., Glen, C. R., Collins, D. R., Molina, M. J., and Zhang, R.: Markedly enhanced

447 absorption and direct radiative forcing of black carbon under polluted urban environments,  
448 Proceedings of the National Academy of Sciences, 113, 4266-4271, 10.1073/pnas.1602310113, 2016.  
449 Qiao, K., Wu, Z., Pei, X., Liu, Q., Shang, D., Zheng, J., Du, Z., Zhu, W., Wu, Y., Lou, S., Guo, S.,  
450 Chan, C. K., Pathak, R. K., Hallquist, M., and Hu, M.: Size-resolved effective density of submicron  
451 particles during summertime in the rural atmosphere of Beijing, China, Journal of Environmental  
452 Sciences, 10.1016/j.jes.2018.01.012, 2018.  
453 Ricchiazzi, P., Yang, S., Gautier, C., and Sowle, D.: SBDART: A Research and Teaching Software  
454 Tool for Plane-Parallel Radiative Transfer in the Earth's Atmosphere, Bulletin of the American  
455 Meteorological Society, 79, 2101-2114, 10.1175/1520-0477(1998)079<2101:sarats>2.0.co;2, 1998.  
456 Seinfeld, J. H., Pandis, S. N., and Noone, K.: Atmospheric Chemistry and Physics: From Air Pollution  
457 to Climate Change, Environment Science & Policy for Sustainable Development, 40, 26-26, 1998.  
458 Stelson, A. W.: Urban aerosol refractive index prediction by partial molar refraction approach,  
459 Environ.sci.technol, 24:11, 1676-1679, 1990.  
460 Tang, I. N., and Munkelwitz, H. R.: WATER ACTIVITIES, DENSITIES, AND REFRACTIVE-  
461 INDEXES OF AQUEOUS SULFATES AND SODIUM-NITRATE DROPLETS OF  
462 ATMOSPHERIC IMPORTANCE, J Geophys Res-Atmos, 99, 18801-18808, 10.1029/94jd01345,  
463 1994.  
464 Tang, I. N.: Chemical and size effects of hygroscopic aerosols on light scattering coefficients, Journal  
465 of Geophysical Research: Atmospheres, 101, 19245-19250, 10.1029/96jd03003, 1996.  
466 Tao, J. C., Zhao, C. S., Ma, N., and Liu, P. F.: The impact of aerosol hygroscopic growth on the single-  
467 scattering albedo and its application on the NO<sub>2</sub> photolysis rate coefficient, Atmos. Chem. Phys., 14,  
468 12055-12067, 10.5194/acp-14-12055-2014, 2014.  
469 Wex, H., Neusüß, C., Wendisch, M., Stratmann, F., Koziar, C., Keil, A., Wiedensohler, A., and Ebert,  
470 M.: Particle scattering, backscattering, and absorption coefficients: An in situ closure and sensitivity  
471 study, Journal of Geophysical Research: Atmospheres, 107, LAC 4-1-LAC 4-18,  
472 10.1029/2000jd000234, 2002.

473 Yue, G. K., Poole, L. R., Wang, P. H., and Chiou, E. W.: STRATOSPHERIC AEROSOL ACIDITY,  
474 DENSITY, AND REFRACTIVE-INDEX DEDUCED FROM SAGE-II AND NMC  
475 TEMPERATURE DATA, *J Geophys Res-Atmos*, 99, 3727-3738, 10.1029/93jd02989, 1994.

476 Zarzana, K. J., Cappa, C. D., and Tolbert, M. A.: Sensitivity of Aerosol Refractive Index Retrievals  
477 Using Optical Spectroscopy, *Aerosol Sci. Technol.*, 48, 1133-1144, 10.1080/02786826.2014.963498,  
478 2014.

479 Zhang, G., Bi, X., Qiu, N., Han, B., Lin, Q., Peng, L., Chen, D., Wang, X., Peng, P., apos, an, Sheng,  
480 G., and Zhou, Z.: The real part of the refractive indices and effective densities for chemically  
481 segregated ambient aerosols in Guangzhou measured by a single-particle aerosol mass spectrometer,  
482 *Atmospheric Chemistry and Physics*, 16, 2631-2640, 10.5194/acp-16-2631-2016, 2016.

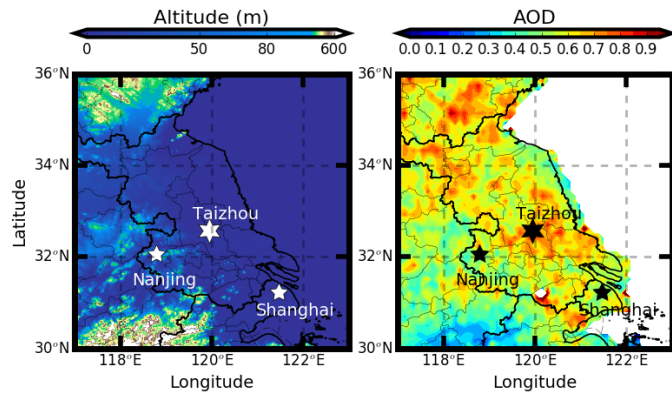
483 Zhao, G., Zhao, C., Kuang, Y., Tao, J., Tan, W., Bian, Y., Li, J., and Li, C.: Impact of aerosol  
484 hygroscopic growth on retrieving aerosol extinction coefficient profiles from elastic-backscatter lidar  
485 signals, *Atmospheric Chemistry and Physics*, 17, 12133-12143, 10.5194/acp-17-12133-2017, 2017.

486 Zhao, G., Zhao, C., Kuang, Y., Bian, Y., Tao, J., Shen, C., and Yu, Y.: Calculating the aerosol  
487 asymmetry factor based on measurements from the humidified nephelometer system, *Atmospheric  
488 Chemistry and Physics*, 18, 9049-9060, 10.5194/acp-18-9049-2018, 2018.

489 Zhao, G., Zhao, W., and Zhao, C.: Method to measure the size-resolved real part of aerosol refractive  
490 index using differential mobility analyzer in tandem with single-particle soot photometer, *Atmospheric  
491 Measurement Techniques*, 12, 3541-3550, 10.5194/amt-12-3541-2019, 2019.

492

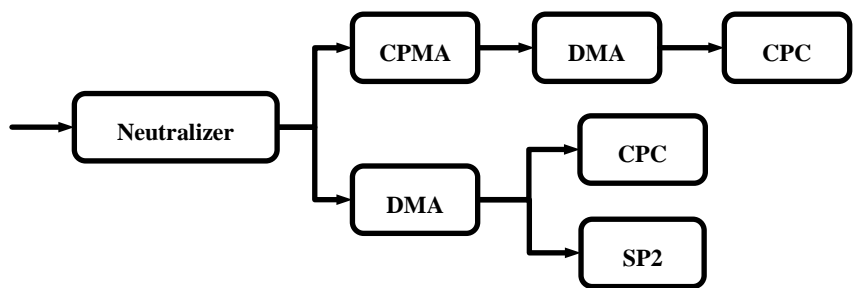
493



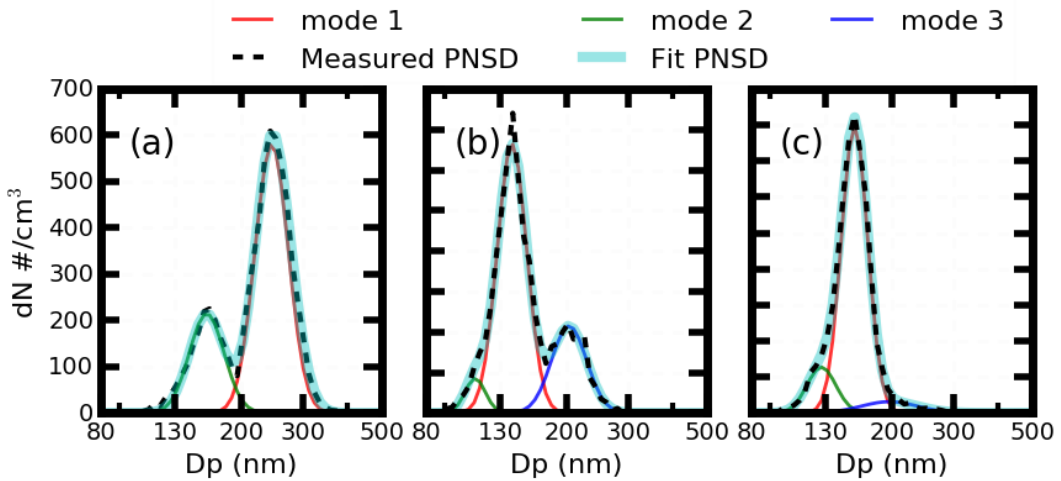
494

495 **Figure 1:** Measurement site of Taizhou (marked with stars). Filled colors represent (a) the  
496 topography of the Jianghuai Plain. (b) the average aerosol optical depth at 550nm during the year of  
497 2017 from Moderate Resolution Imaging Spectroradiometer onboard satellite Aqua.

498

500 **Figure 2.** Schematic of the instrument setup.

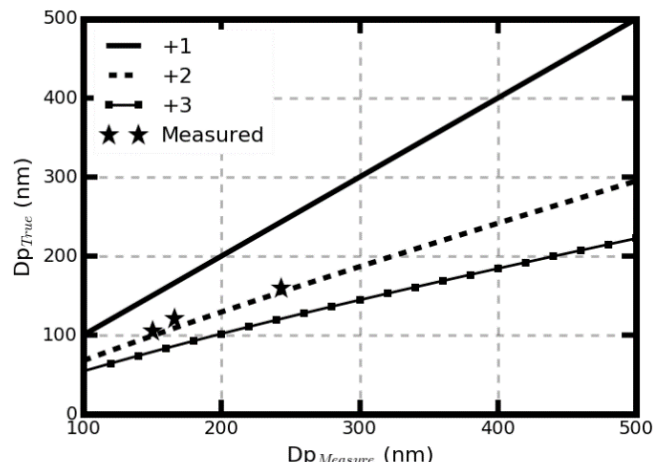
503



504

505 **Figure 3.** The measured aerosol PNSD (black dotted line), fit aerosol number PNSD (blue solid line),  
506 and fit aerosol PNSD at three different mode in different colors that passed through the CPMA. Panel  
507 (a) (b) (c) corresponding to the aerosol mass concentrations of 12, 1 and 1.45 fg respectively.

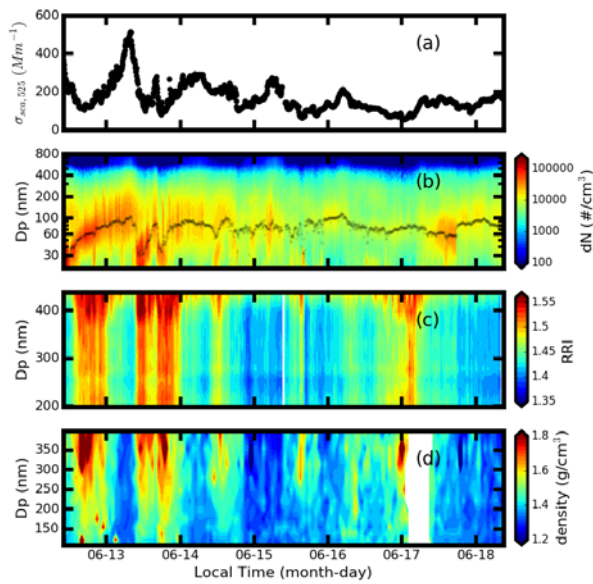
508



511 **Figure 4.** The relationship between the measured diameter by the DMA and the calculated aerosol  
512 diameter of different charges in the CPMA-SMPS system.

514

515



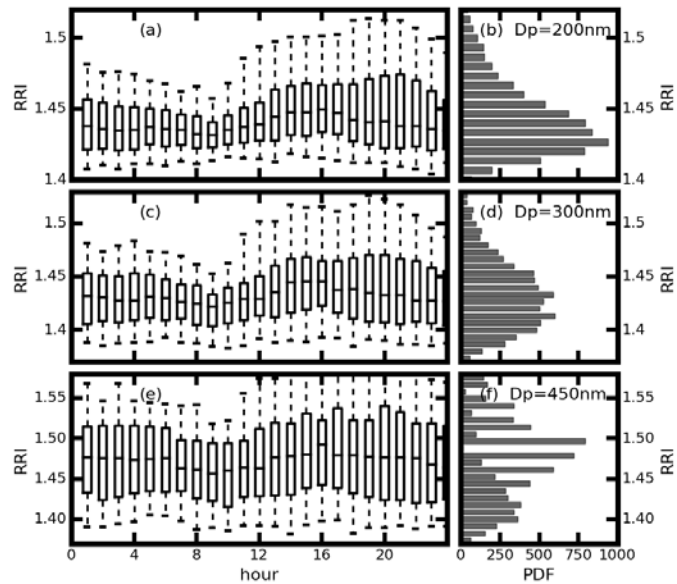
516

517

**Figure 5.** Time series of the measured (a) size-resolved RRI in filled color,  $\sigma_{\text{sca}}$  at 525nm in black dotted line and (b) the size-resolved  $\rho_{\text{eff}}$ .

518

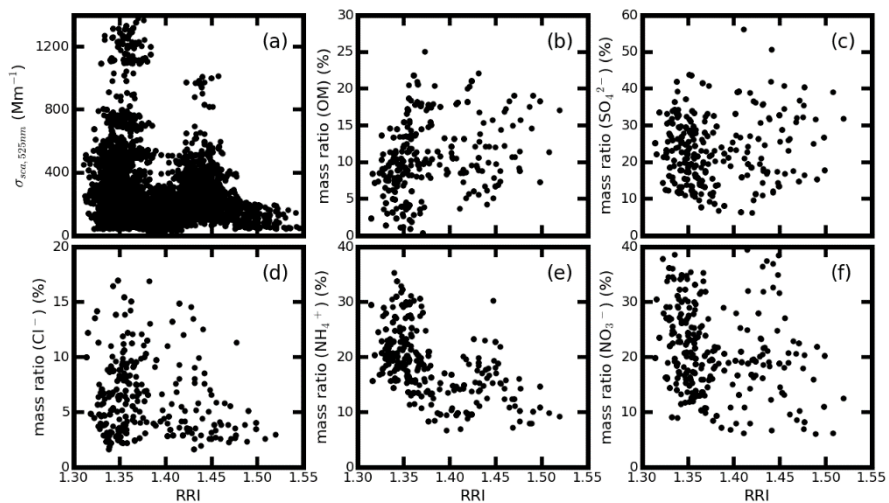
519



520

521 **Figure 6.** Daily variations of the RRI (a), (c) (e), and the probability distribution of the measured  
 522 RRI (b), (d) (f) for the (a), (b) 200 nm, (c), (d) 300 nm, and (e), (f) 450nm aerosol respectively. The  
 523 box and whisker plots represent the 5<sup>th</sup>, 25<sup>th</sup>, 75<sup>th</sup> and 95<sup>th</sup> percentiles.

524



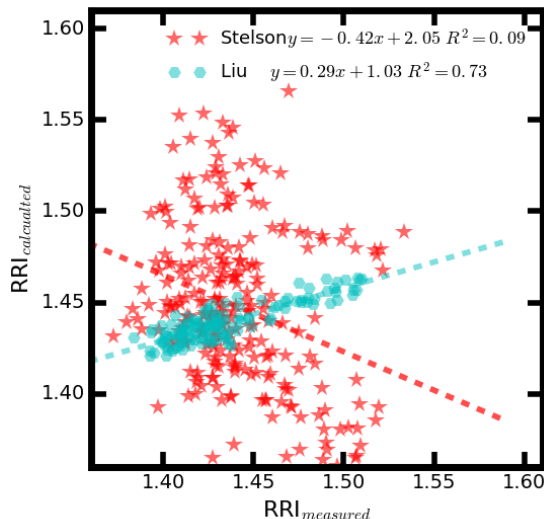
525

526

**Figure 7.** Comparison the measured RRI at 300nm with the measured (a)  $\sigma_{\text{sca}}$  at 525nm, mass

527 fraction of (b) OM, (c)  $\text{SO}_4^{2-}$ , (d)  $\text{Cl}^-$ , (e)  $\text{NH}_4^+$  and (f)  $\text{NO}_3^-$ .

528

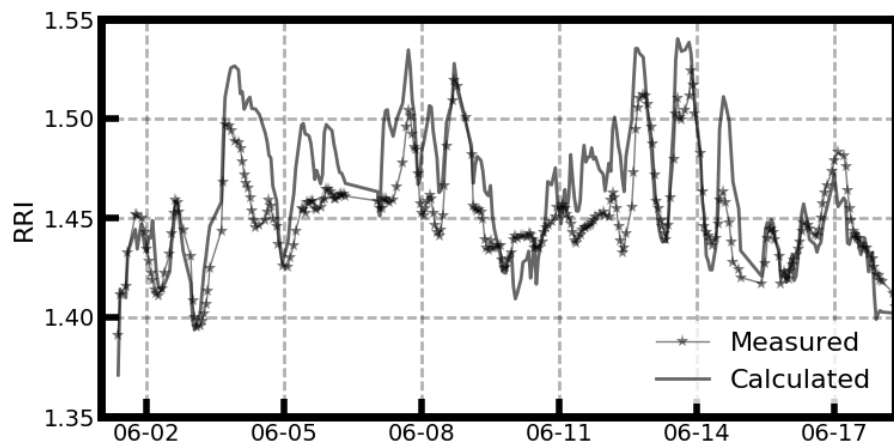


529

530 **Figure 8.** Comparison between the measured RRI and calculated RRI using the main aerosol  
 531 chemical component by applying the method of Stelson (1990) (in red star) and parameterization  
 532 scheme proposed by Liu and Daum (2008) (in cyan hexagon).

533

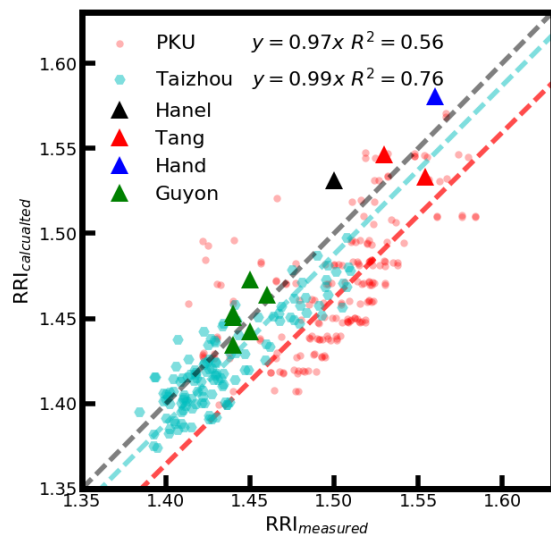
534



535

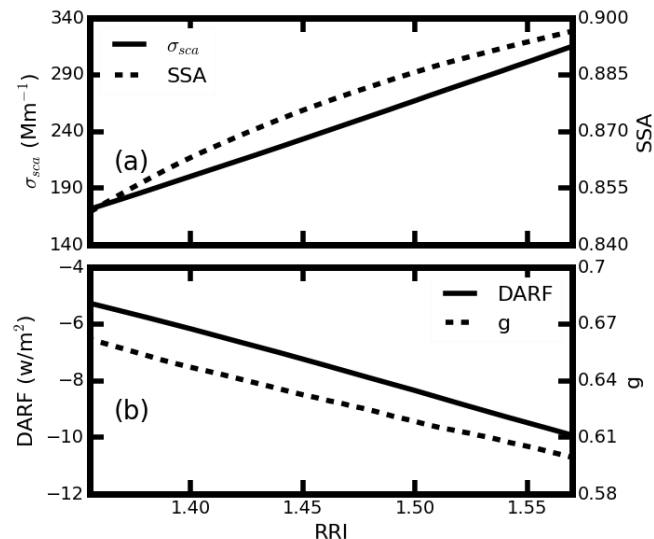
536 **Figure 9.** Time series of the measured RRI at 250 nm and the calculated RRI using the aerosol bulk  
537 aerosol optical properties.

538



541 **Figure 10.** Comparison between the measured and calculated RRI for different at PKU (in red circle)  
 542 and Taizhou (in cyan hexagon) station. The triangle in black , red, blue and green corresponding the  
 543 data from Hänel (1968), Tang (1996), Hand and Kreidenweis (2002), and Guyon et al. (2003)  
 544 respectively. The black dashed line is the 1:1 line.

546



547

548 **Figure 11.** Variations of the estimated (a)  $\sigma_{sca}$  in solid line, SSA in dotted line, (b)  $g$  in dotted  
549 line, and DARF in solid line for different aerosol RRI.

550